MELBA Journal Machine Learning for Biomedical Imaging

GazeLT: Visual attention–guided long-tailed disease classification in chest radiographs

Moinak **Bhattacharya** [1], Gagandeep **Singh** [2], Shubham **Jain** [3], Prateek **Prasanna** [1],

1 Department of Biomedical Informatics, Stony Brook University, NY, US, 11790
2 Department of Radiology, Columbia University, NY, US, 10027
3 Department of Computer Science, Stony Brook University, NY, US, 11790

Abstract

In this work, we present *GazeLT*, a *human visual attention integration-disintegration approach* for long-tailed disease classification. A radiologist's eye gaze has distinct patterns that capture both fine-grained and coarser level disease related information. While interpreting an image, a radiologist's attention varies throughout the duration; it is critical to incorporate this into a deep learning framework to improve automated image interpretation. Another important aspect of visual attention is that apart from looking at major/obvious disease patterns, experts also look at minor/incidental findings (few of these constituting long-tailed classes) during the course of image interpretation. *GazeLT* harnesses the temporal aspect of the visual search process, via an integration and disintegration mechanism, to improve long-tailed disease classification. We show the efficacy of *GazeLT* on two publicly available datasets for long-tailed disease classification, namely the NIH-CXR-LT (n=89237) and the MIMIC-CXR-LT (n=111898) datasets. GazeLT outperforms the best long-tailed loss by 4.1% and the visual attention-based baseline by 21.7% in average accuracy metrics for these datasets. Our code is available at `https://github.com/lordmoinak1/gazelt`.

Keywords

Eye gaze, Long-tailed classification, Chest X-ray.

Article informations

`https://doi.org/10.59275/j.melba.2026-d8c8`
Volume 2026, Received: 2025-08-01, Published 2026-02-02
Corresponding author: moinak.bhattacharya@stonybrook.edu

©2026 Bhattacharya, Singh, Jain and Prasanna. License: CC-BY 4.0

Check for updates

aXiv:2508.09478v2 [cs.CV] 25 Jul 2026

1. Introduction

Eye gaze patterns are important in understanding the visuo-cognitive process underlying a radiologist's interpretation of medical images (Van der Gijp et al. (2017)). Visual patterns can be attributed to maintaining, manipulating, and retaining information based on past and current observations (Logie (2003)). This information can range from coarse trivial attention to fine-grained non-trivial attention patterns. Coarse attention patterns may arise due to non-salient abnormalities, often not relevant to the diagnosis of any particular disease whereas fine-grained patterns are associated with salient abnormalities that contain information of specific disease patterns and location. Gaze patterns are direct implications of the perception of a salient object in the search view based on the object's physical appearance and location (Jian et al. (2021)). The temporal aspect of this search becomes critical as, with time, more information gets stored in memory and that directly affects the future gaze patterns (Drew et al. (2017)). As a simple example, in a find-an-object puzzle/game, a person starts looking from the top left corner and after a detailed search concludes that the object-of-interest is not in that particular region; in the future, the probability of searching in that region is lower than searching in other regions. Again, before moving to any other region for further fine-grained search, the person prefers to have a global view of the entire region, and based on random understanding, the next region is selected. This approach of global random search is akin to disintegration attention (Dieter and Tadin (2011)) and the fine-grained search can be compared to the integration attention (Ferreira and Dias (2014)) in human psychology. We present a method to incorporate the integration and disintegration attentions into a deep learning (DL) framework for better-informed and more interpretable decision-making. This is important as DL models often tend to focus on

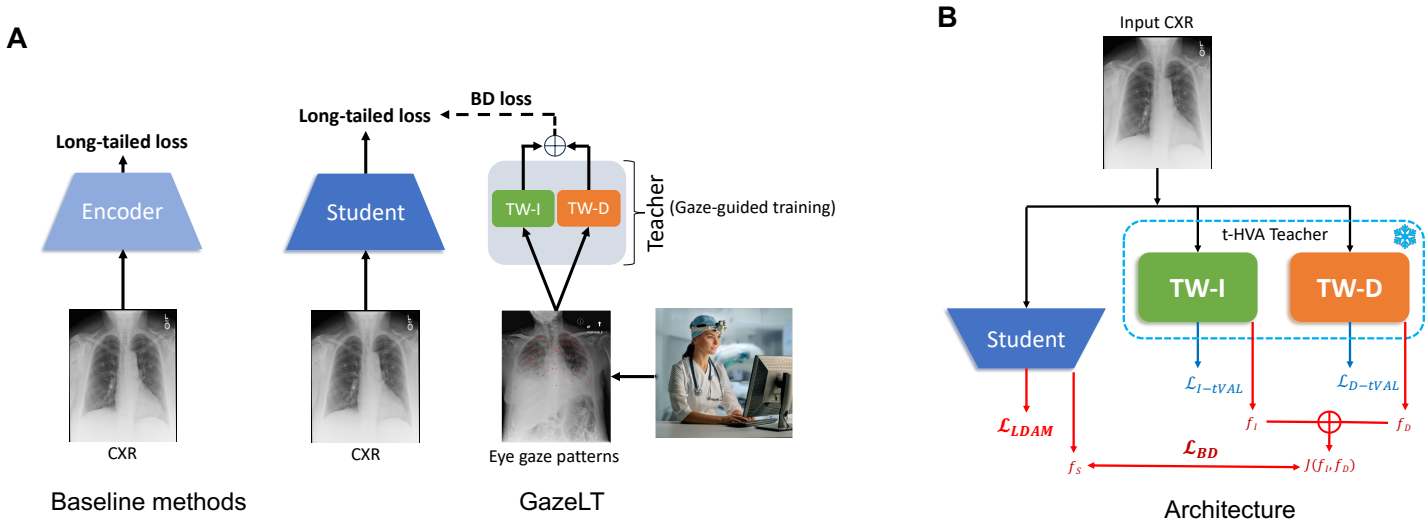

Figure 1: A. Baseline methods use a vision encoder with long-tailed losses $\mathcal{L}_{LT}$ whereas GazeLT uses a teacher-student framework where the teacher is trained with radiologists' visual attention patterns and then the student is trained by distilling the knowledge from the teacher using $\mathcal{L}_{BD}$ and the long-tailed loss $\mathcal{L}_{LT}$, B. GazeLT is a teacher-student framework. The t-HVA teacher has two components, TW-I and TW-D. The TW-I is trained using $\mathcal{L}_{I-tVAL}$ and the TW-D is trained using $\mathcal{L}_{D-tVAL}$. During student training, the f_I and f_D from t-HVA are fused and distilled to the student using $\mathcal{L}_{BD}$.

disease-irrelevant features for disease predictions. Radiologists' eye gaze patterns, collected during diagnosis, can be used to better guide a DL model to focus on disease-relevant regions.

Improving the interpretability of DL models in medicine has been an active area of research (Salahuddin et al. (2022)). DL models in radiology often tend to learn shortcuts (Ma et al. (2023)) or look at irrelevant regions while making predictions (Zhang et al. (2023a)). One approach to address this involves the incorporation of clinical experts' visual search patterns into the model (Bhattacharya et al. (2022a,b); Bhattacharya and Prasanna (2024); Bhattacharya et al. (2024)). This *clinician-in-the-loop* strategy is gaining prominence. Recent works show that DL models perform better when clinicians' feedback is incorporated into the decision-making pipeline (Feng et al. (2022)). In this work, we propose a novel strategy for integrating clinical experts' visual patterns into DL models. More specifically, our model is explicitly trained with the integration and disintegration attention patterns of radiologists to make a diagnosis. This helps the model make more clinically accurate predictions. We demonstrate the efficacy of long-tailed classification tasks in pulmonary disease classification by integrating the eye gaze patterns of radiologists.

Long-tailed classification in medical imaging is a challenging problem. This challenge arises from the disparity in prevalence between common diseases, which are relatively limited in number and easily observable in images such as chest radiographs, and rare diseases, which exhibit a considerably higher variety (Zhou et al. (2021); Paul et al. (2021)). For example, in most of the chest radiography datasets, diseases like Pneumothorax, Atelectasis, Infiltration, etc., are common pathologies present in $> 60\%$ of the total patients, whereas diseases like Pneumomediastinum, Subcutaneous Emphysema, Pneumoperitoneum, etc., are rare pathologies present in $< 1\%$ of the total patients. The common disease types are called head classes and the rare disease types are called tail classes (Zhang et al. (2023b)). DL models have been shown to perform better in discriminating the head classes and exhibit poor performance in identifying/discriminating tail classes (Holste et al. (2022)). Recently, several methods have been proposed in the fields of imbalanced learning (Zhou et al. (2021)), and few-shot learning (Feng et al. (2021)) to deal with long-tailed classification. However, none of these use clinicians' feedback, in any form, to improve long-tailed learning. We hypothesize that, for long-tailed classification, experts' visual patterns are of prime importance. Radiologists, while reading an image, fixate on obvious abnormalities which are the head classes in the datasets, and also scan through other incidental findings, some of which may correspond to the tail classes (Figure 4).

Our rationale for decomposing the 'static' nature of attention as used in previous studies (Stember et al. (2020); Bhattacharya et al. (2022a,b); Bhattacharya and Prasanna (2024); Bhattacharya et al. (2024)) to a 'temporally re-

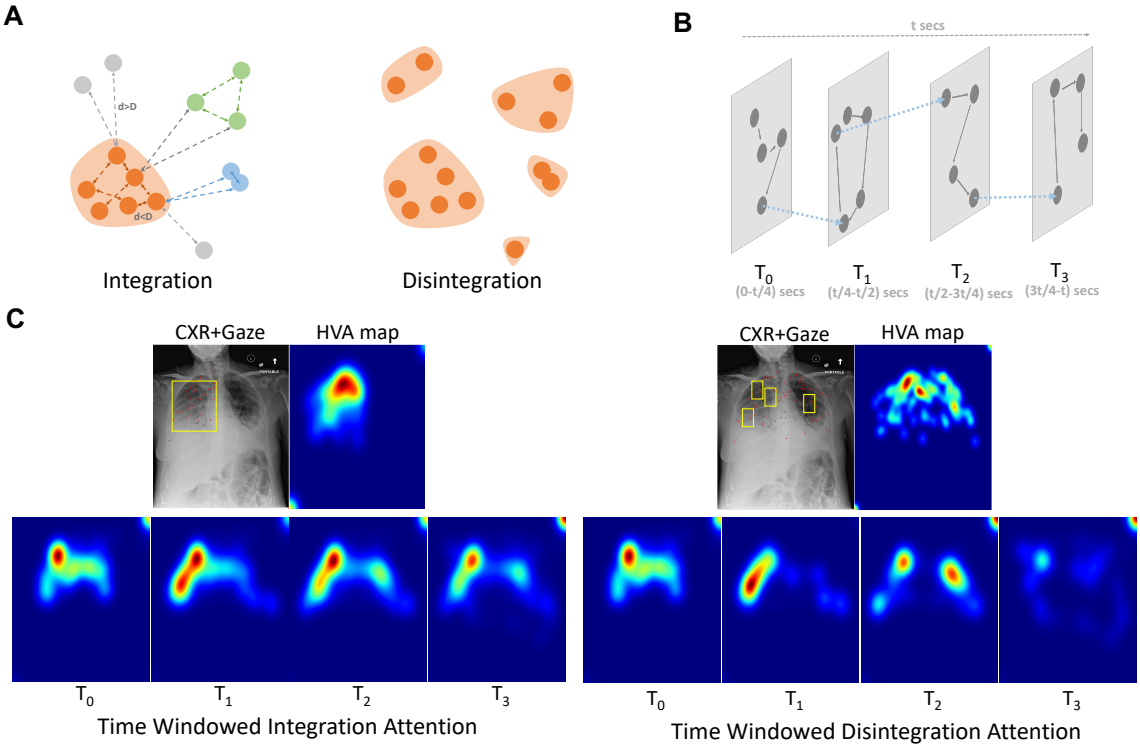

Figure 2: A. Integration and disintegration of eye gaze points, with orange clusters representing distinct attention calculation mechanisms, B. Partitioning of eye gaze points into specific time intervals for temporal attention modeling, C. Time Windowed HVA maps. The HVA maps at different timepoints, T0, T1, T2 and T3, for Integration and Disintegration are shown.

solved' form stems from this dynamic nature of viewing patterns of radiologists during diagnosis. This motivates us to compartmentalize the gaze patterns into windows based on durations. We hypothesize that the gaze patterns in these individual windows fixate, partially or wholly, on individual disease-relevant regions. These regions have context-rich disease information of the individual head, medium, and tail classes. Hence, the integration of these time-windowed human visual attentions into a deep learning framework can facilitate long-tailed learning. In this work, we present GazeLT, a novel temporal visual attention-guided teacher-student deep learning framework for long-tailed classification (Figure 1).

To the best of our knowledge, no other work has investigated the impact of experts' visual attention in long-tailed learning. Our work is based on the premise that temporal visual attention of radiologists can infuse auxiliary diagnostic information into a DL framework to help improve long-tailed classification. Previous works have focused on the static nature of human visual attention (Stember et al. (2020); Bhattacharya et al. (2022a,b)). We argue that more detailed and contextual clinical diagnostic information can be retrieved if we decompose this 'static' nature of radiologists' attention computation into a 'temporally resolved' form. The main contributions of this paper are as follows:

- We harness the temporal aspect of the visual search process by developing a novel Time Windowed Integration and Disintegration approach to capture the fine-grained and coarse attention patterns. We propose novel Visual Attention Loss (VAL) functions that help the deep learning model to learn the visual attention patterns,
- We propose a teacher-student framework where the teacher is trained with time-windowed visual attention and distills the features to a student that is finetuned for downstream long-tailed classification, and
- We show the efficacy of our method on two medical long-tailed classification benchmarks, NIH-CXR-LT and MIMIC-CXR-LT.

We observe that radiologists' eye gaze patterns offer valuable insights into disease characteristics, particularly within the long-tail distribution of diagnostic categories. Leveraging these patterns in machine learning models presents a promising strategy for addressing the challenges of long-tailed disease classification. To the best of our knowledge, no prior work has incorporated radiologists' gaze behavior to specifically mitigate the long-tail classification problem. Our

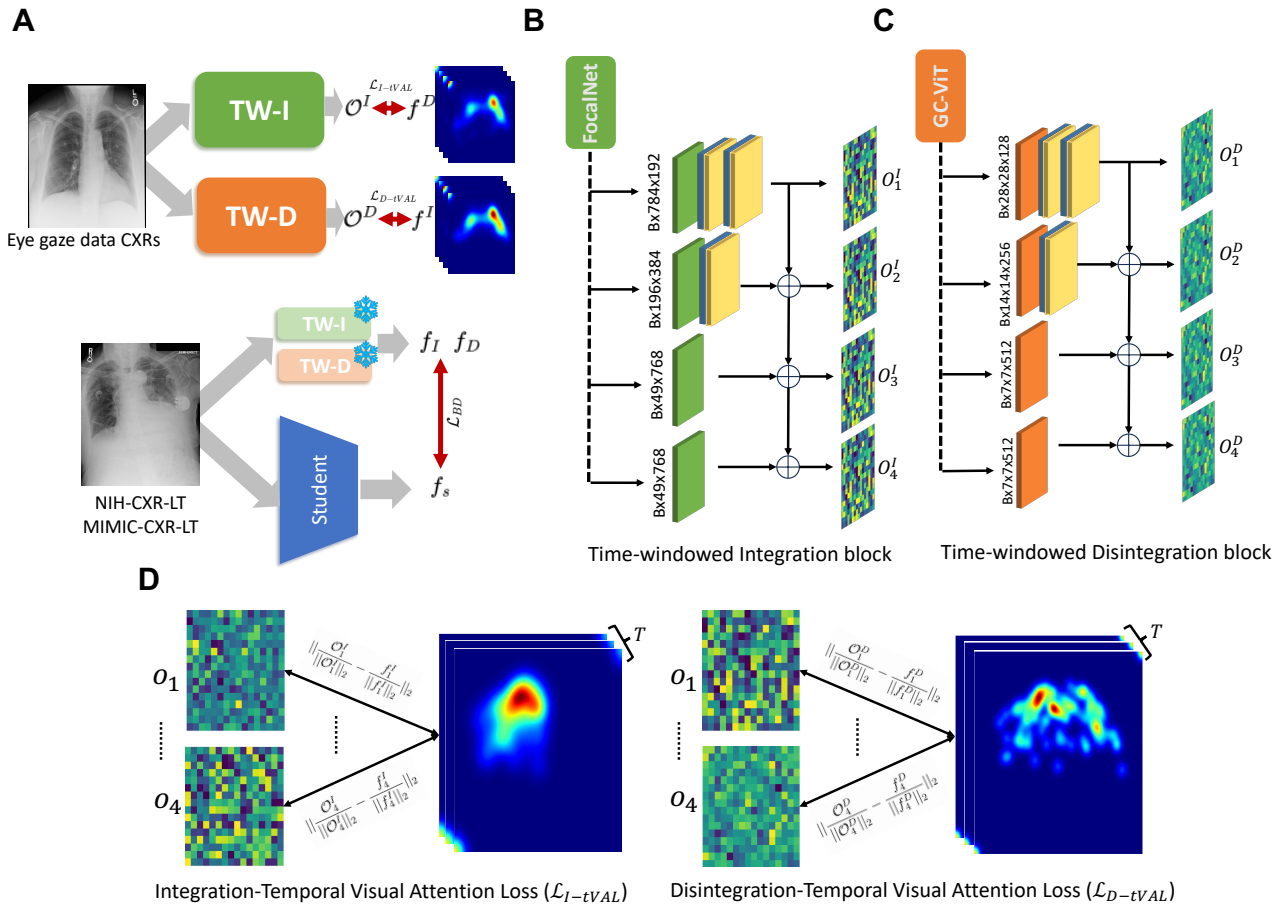

Figure 3: A. Overall training pipeline illustrating the two-stage process: (i) the teacher network is pretrained using raw gaze points segmented into n time windows to encode temporal visual attention via TW-I and TW-D modules; (ii) the student model is trained with frozen teacher supervision through feature-level distillation. B. TW-I block is a FocalNet transformer architecture from which the integration feature outputs $\mathcal{O}_i^I$ are obtained using a decoder, C. TW-I block is a GC-ViT transformer architecture from which the disintegration feature outputs $\mathcal{O}_i^D$ is obtained using a decoder. D. Time Windowed Visual Attention Loss (tVAL). The loss for the TW-I block, $\mathcal{L}_{I-tVAL}$, and the loss for the TW-D block, $\mathcal{L}_{D-tVAL}$.

proposed approach demonstrates improved performance on publicly available datasets for long-tailed classification of pulmonary diseases.

2. Related Works

2.1 Eye gaze in medical image analysis

Eye gaze tracking has emerged as a powerful tool in various medical applications, such as disease classification (Bhattacharya et al. (2022a,b)) and segmentation (Wang et al. (2023)), across multiple modalities including radiology (Stember et al. (2020)), pathology (Sudin et al. (2022)), retinopathy (Clark et al. (2019)), and ECG analysis (Sqalli et al. (2022); Tahri Sqalli et al. (2021)). The integration of eye gaze in general computer vision tasks has shown success in several downstream tasks such as object detection (Smith et al. (2013); Cho and Kang (2021)), image segmentation (Amrouche et al. (2018); James et al. (2007); Shi et al. (2017)), action localization (Shapovalova et al. (2013); Mathe and Sminchisescu (2014)), and activity recognition (Courtemanche et al. (2011); Min and Corso (2021)). Building on these advancements, recent research has focused on utilizing gaze patterns from medical professionals, such as radiologists and pathologists, to improve the diagnostic performance of ML models and reduce diagnostic errors (Roshan et al. (2023)). Specifically, teacher-student knowledge distillation models have demonstrated the potential of leveraging gaze data to improve disease diagnosis (Bhattacharya et al. (2022a,b)). Eye gaze patterns have also been effectively integrated with deep learning frameworks, including graph neural networks (Wang et al. (2024)), vision transformers (Ma et al. (2023); Bhattacharya et al. (2022b)), etc. In recent advances, eye gaze data have been used in medical image generation (Bhattacharya and Prasanna (2024); Bhattacharya et al. (2024)). However,

the use of radiologists' eye gaze patterns to enhance long-tailed classification in deep learning remains underexplored. These patterns, which highlight rare and incidental findings, can guide models to better predict tail classes. We propose a method that leverages gaze information to improve long-tailed learning performance.

2.2 Long-tailed disease classification

Long-tailed learning has emerged as a critical challenge in medical imaging due to the inherent class imbalance in clinical datasets. Rare pathologies are often underrepresented compared to common conditions, leading to performance degradation in standard deep learning models trained with conventional loss functions and sampling strategies. While long-tailed learning has been extensively studied in natural image domains using techniques such as re-sampling (Wang et al. (2020); Estabrooks et al. (2004); Zhang and Pfister (2021)) and re-weighting (Ren et al. (2020); Elkan (2001); Jamal et al. (2020); Tan et al. (2021, 2020)), these approaches remained largely unexplored in medical imaging until recent advancements. In medical imaging, several studies have begun addressing class imbalance through modifications to loss functions. For example, a unified focal loss was proposed to tackle class imbalance in medical image segmentation (Yeung et al. (2022)). Weighted class-balanced loss (Yue et al. (2022); Roy et al. (2022)) and loss re-weighting techniques (Shirokikh et al. (2020)) have also demonstrated promise in mitigating imbalance. However, only a limited number of methods have specifically addressed the challenges posed by the long-tailed distribution of disease classes. Recently, novel approaches have emerged to address long-tailed learning for medical image classification. Balanced-MixUp (Galdran et al. (2021)) addresses long-tailed distributions by mixing instance-based and class-based samples within the dataset. Another method groups rare classes into subsets based on prior knowledge and employs knowledge distillation to learn these subsets (Ju et al. (2021)). Additionally, Zhang et al. (2021) proposed resampling tail classes using a memory module combined with a re-weighting loss function to enhance long-tailed classification performance. Furthermore, a robust asymmetric loss function has been introduced, which regularizes the loss using the Hill loss approach for multi-label long-tailed learning (Park et al. (2023)).

Despite these advancements, current methods still struggle with the accurate classification of long-tailed disease distributions. While some recent approaches attempt to address this issue through modified loss functions, they often overlook the potential of radiologist-guided disease pattern learning. For instance, integrating eye-gaze data could help deep learning models focus on critical regions, particularly for rare diseases. In this work, we propose a novel approach that incorporates radiologist eye-gaze patterns to improve long-tailed thoracic disease classification.

3. Method

Algorithm 1 Generation of Visual Attention Heatmaps from Eye-Gaze Fixations

Require: Chest X-ray image I, gaze fixation points $G = \{(x_i, y_i)\}_{i=1}^{N}$, chest bounding box $B = (x_{min}, y_{min}, x_{max}, y_{max})$

Ensure: Visual attention heatmap H

Load image I and obtain image dimensions (H_I, W_I)
Initialize empty fixation set F
for each fixation point (x_i, y_i) in G **do**
  if $x_{min} \leq x_i \leq x_{max}$ AND $y_{min} \leq y_i \leq y_{max}$ **then**
    Add (x_i, y_i) to F
  end if
end for
Append boundary points $(0, 0)$ and (W_I, H_I) to F
Global Attention:
Generate 2D histogram H_g from fixation coordinates in F
Apply Gaussian smoothing:

$$H_g = \text{GaussianFilter}(H_g, \sigma_g)$$

Focal Attention:
Cluster fixation points using K-means ($k = 2$)
Select dominant fixation cluster C
Generate histogram H_f from cluster C
Apply Gaussian smoothing:

$$H_f = \text{GaussianFilter}(H_f, \sigma_f)$$

Overlay heatmap on chest X-ray image
return Heatmap visualization H

The proposed method is shown in Figure 1. We implement a teacher-student-based knowledge distillation (KD) framework in which the teacher is trained with snapshots of radiologist's eye gaze patterns at different time points called temporal-Human Visual Attention (t-HVA). During inference, we freeze the pre-trained teacher and only train the student for long-tailed thoracic disease classification. In Section 3.1, we discuss the Time Windowed Integration and Disintegration blocks along with the loss functions. In Section 3.2, we discuss how the feature maps of t-HVA are calculated and how the teacher is trained. Finally, in Section 3.3, we discuss the KD from the t-HVA teacher to the student for long-tailed classification.

Preliminary. For computing t-HVA, we use the CXR image $\mathcal{I} \in \mathbb{R}^{H \times W \times C}$, where H is the height, W is the width, and C is the number of channels of the image, and the

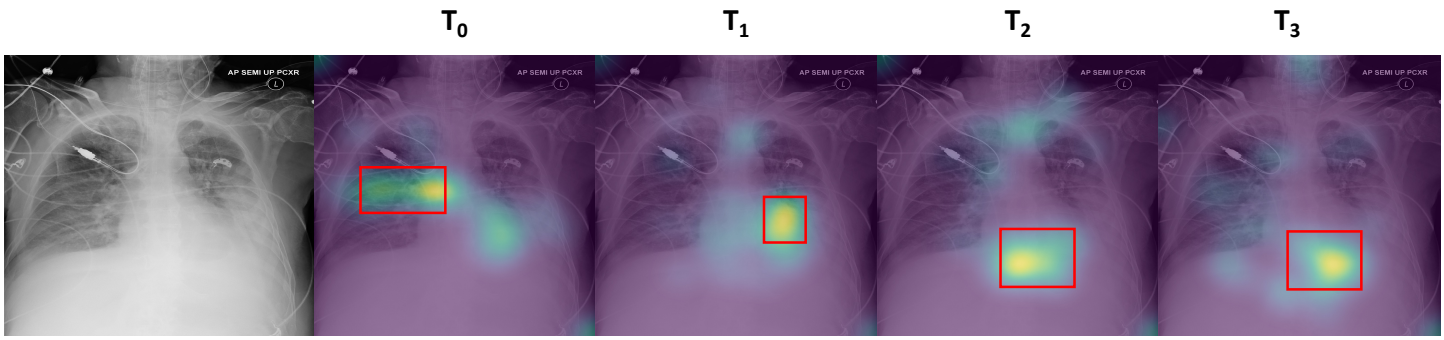

Figure 4: Radiologists' interpretation: Heatmap visualization of model attention across four timepoints (T_0, T_1, T_2, T_3) on chest X-ray images. The red boxes highlight regions of interest as identified by the model. The focus shifts from areas associated with atelectasis, classified as the 'head' class, at T_0 and T_1, to areas related to a hiatal hernia, classified as the 'tail' class, at T_2 and T_3.

corresponding radiologist eye gaze pattern $\mathbb{G} \in \mathbb{R}^{(\mathcal{F},\mathcal{T})}$. Here, $\mathcal{F}$ are the eye gaze fixations over time $\mathcal{T}$ collected for CXR image $\mathcal{I}$. During inference, we only have a CXR image $\hat{\mathcal{I}} \in \mathbb{R}^{H\times W\times C}$ for which we need to predict a label y. Here, the objective is a long-tailed classification task where y constitutes the *head*, *medium*, and *tail* classes.

3.1 Time Windowed Integration-Disintegration

To calculate integration attention, we define a threshold distance between fixation points and select all points within this distance to designate as the main attention region. All other points are assigned to substitute attention regions. Together, the main and substitute attention regions form the integration attention. Gaussian filtering with a sigma value of 64 is then applied to these regions to generate the integration attention heatmap. In contrast, for disintegration attention, Gaussian filtering is applied directly to the raw fixation points with a sigma value of 128, producing the disintegration attention heatmap (Figure 2.A). The duration of a radiologist's image viewing, referred to as fixation duration, is divided into n equal time partitions (in our case n=4). For instance, if the total fixation duration is 60 seconds, each partition would span 15 seconds. The fixation points are then distributed across these four time windows. For example, if there are 100 fixation points in total, there might be 20 points in the first 15-second window, 40 points in the next 15-second window, and so forth (Figure 2.B). Within each time window, integration and disintegration attention are calculated using the corresponding fixation points. This integration (I) and disintegration (D) attention calculation is shown in Figure 2.C. The integration attention is represented as f^I and the disintegration attention is representation as f^D. For different time windows, the integration attention HVA maps and the disintegration attention HVA maps are shown in Figure 4, respectively.

3.2 Training

We train our proposed model using a teacher-student approach (Figure 3). In this framework, the teacher block is trained using radiologists' eye gaze patterns, while the student block is trained for long-tailed classification. The teacher block consists of Time Windowed Integration (TW-I) and Time Windowed Disintegration (TW-D) blocks. The TW-I block learns to aggregate temporally distributed visual attention maps from the eye-gaze fixation points by computing an integration attention loss between its attention maps and those attention of the intermediate layers from the teacher model, which processes full temporal sequences. This encourages the TW-I block to mimic how radiologists integrate gaze information over time to arrive at diagnostic decisions. Conversely, the TW-D block learns to decompose global diagnostic cues into temporally localized attention maps, guided by a disintegration attention loss that aligns its outputs with the temporal structure of the teacher's attention. This dual mechanism ensures that the student model can both synthesize and localize relevant temporal features, enabling more robust learning under long-tailed label distributions. The TW-I block contains four sub-blocks, each utilizing Focal Attention to compute attention. Focal Attention computes attention using the focal modulation mechanism and hence attention for each TW-I block is computed sequentially (Figure 3.A). Similarly, the TW-D block also comprises four sub-blocks, with each layer computing attention using global context attention (Figure 3.B). The CXR image is fed as input to both the TW-I and TW-D blocks, where each block processes the image through four sequential attention layers. The output of the t-th layer in the TW-I block is denoted as $\mathcal{O}_t^I$, and similarly, the output of the t-th layer in the TW-D block is denoted as $\mathcal{O}_t^D$, for $t \in 1, 2, 3, 4$. The TW-I and TW-D blocks are trained with their respective visual attention losses, $\mathcal{L}_{I\text{-}tVAL}$ and

$\mathcal{L}_{D\text{-}tVAL}$, which enforce alignment between the predicted attention maps and radiologists' gaze-derived attention, guiding each block to model temporal integration and disintegration of diagnostic cues effectively. This loss function minimizes the distance between the intermediate layers of the TW blocks and the ground truth human visual attention (HVA) windows (Figure 3.C).

$$\mathcal{L}_{I-tVAL} = \sum_{i=1}^{L} \left\| \frac{\mathcal{O}_t^I}{\|\mathcal{O}_t^I\|_2} - \frac{f_t^I}{\|f_t^I\|_2} \right\|_2 \tag{1}$$

$$\mathcal{L}_{D-tVAL} = \sum_{i=1}^{L} \left\| \frac{\mathcal{O}_t^D}{\|\mathcal{O}_t^D\|_2} - \frac{f_t^D}{\|f_t^D\|_2} \right\|_2 \tag{2}$$

where $\mathcal{O}^I$ is the output of the TW-I block and $\mathcal{O}^D$ is the output of the TW-D block.

3.3 Knowledge Distillation

For long-tailed classification, we distill knowledge from a teacher model, pretrained with radiologists' eye gaze data, to a student model. The teacher-Human Visual Attention model (t-HVA) comprises the Time Windowed Integration (TW-I) and Time Windowed Disintegration (TW-D) blocks, which together encode both global and localized temporal gaze patterns of radiologists. The student model, in contrast, adopts a standard ResNet architecture. During training, the pretrained teacher's weights are frozen and used to guide the student via feature-level supervision. Specifically, the fused representations from TW-I and TW-D are transferred to the student through knowledge distillation. This setup ensures that the student not only learns discriminative features from limited data but also inherits the diagnostic priors embedded in expert gaze patterns, while being trained with a long-tailed loss tailored to handle class imbalance. The CXR image is simultaneously input to both the student block and the frozen teacher block, producing feature representations f_s and $\{f_I, f_D\}$, respectively. Here, f_I is the feature from the frozen TW-I and f_D is the feature from the frozen TW-D. The knowledge distillation loss facilitates this process by transferring the joint representation from the teacher block ($J(f_I, f_D)$) to the student block (f_s), minimizing the Bhattacharyya distance between their probability distributions. The feature maps extracted from the teacher and student networks are first normalized using a softmax operation to obtain probability distributions over spatial locations. These normalized distributions are then used to compute the Bhattacharyya distance. The final student model training incorporates a combination of a Label-Distribution-Aware Margin (LDAM) loss ($\mathcal{L}_{LDAM}$) and knowledge distillation loss ($\mathcal{L}_{BD}$), ensuring effective learning from the teacher model while addressing class imbalance.

$$\mathcal{L}_{BD} = -ln\left(\int \sqrt{f_s * J(f_I, f_D)} \right) \tag{3}$$

$$\mathcal{L}_{LDAM} = -\log \frac{e^{z_y - \Delta_y}}{e^{z_y - \Delta_y} + \sum_{j \neq y} e^{z_j}} \tag{4}$$

where z_y is the score of the class y and Δ_y is the margin for the class y. Finally, the student loss, $\mathcal{L}_s$ is defined as $\mathcal{L}_s = \mathcal{L}_{LDAM} + \lambda \mathcal{L}_{BD}$.

4. Implementation

4.1 Dataset Curation

We utilize eye gaze fixation data from the EGD-CXR and REFLACX datasets. The EGD-CXR dataset contains eye gaze data from one radiologist, whereas the REFLACX dataset contains multiple radiologists' eye gaze data. The corresponding chest X-ray (CXR) images for these eye gaze datasets are obtained from the MIMIC-CXR-JPG dataset. The eye gaze data is used for training the teacher model. For long-tailed classification experiments, we employ the publicly available NIH-CXR-LT and MIMIC-CXR-LT datasets. We adhere to the standard training, balanced testing, and test splits (Holste et al. (2022)) (Details in Supplementary Figure 6).

4.2 Model Hyperparameters

Fixation points within the chest bounding box are clustered using K-means (Euclidean distance, 10 restarts), and the cluster with lower spatial variance is designated as focal attention. The implicit distance threshold ($D_k = \max_i |\mathbf{x}_i - \boldsymbol{\mu}_k|_2$) is determined by K-means without manual tuning. Fixation density maps are constructed via 2D histograms followed by Gaussian smoothing with $\sigma = 128$ for integration and $\sigma = 64$ for disintegration, selected through validation grid search over {32, 64, 96, 128, 160}. The global teacher is GC-ViT-Tiny (depths=[3,4,19,5], heads= $[2, 4, 8, 16]$, dim=64, window sizes= $[7, 7, 14, 7]$, MLP ratio=3, drop path=0.2), initialized with ImageNet-1K weights. The focal teacher is FocalNet-Tiny-SRF (depths =[2,2,6,2], dim=96), also ImageNet pretrained. Both teachers are adapted to single-channel CXR by averaging RGB weights in the first convolution and replacing the classification head. The student network is ResNet-50 (ImageNet pretrained), optimized with SGD (momentum=0.9, weight decay=1e-4, initial LR=1e-3 with cosine decay, batch size= 32), with distillation applied at Layer3 and Layer4 using 1×1 feature projection before the Bhattacharyya loss.

4.3 Evaluation Metrics

We report different metrics based on the test set distribution and task type. For the balanced test set, we report

average accuracy (↑), computed as the unweighted mean of per-class accuracies. In addition to the overall average accuracy, we report the group-wise average accuracy, calculated as the mean of the accuracies for the head, medium, and tail class groups. This metric captures how well the model performs across different class frequency regimes.
For the imbalanced test set, which reflects the real-world long-tailed distribution, we report balanced accuracy (↑), which averages recall across all classes and reduces the bias toward frequent classes.
For multiclass classification experiments, we report four metrics: balanced accuracy (↑), Matthews Correlation Coefficient (MCC) (↑), Area Under the ROC Curve (AUC) (↑), and Weighted F1 Score (wF1) (↑). These metrics collectively provide a comprehensive evaluation of model performance across balanced, imbalanced, and multiclass settings.

4.4 Experiments

The time windows are computed by splitting the entire duration of the eye gaze collection process into 4 equal windows. These splits are done based on time duration. For TW-I training, we use a learning rate (lr) of $1e-4$ and train for 100 epochs. For TW-D training, we use a lr of $5e-4$ and train for 250 epochs. For both, we use Adam optimizer with StepLR scheduling (step size=10. γ=0.1). For student training, we train for 100 epochs with a lr of $1e-4$ and Adam optimizer. We train on a single Quadro RTX 8000 (48 GB) with a batch size of 256.

4.5 Statistical Analysis

We employed a comprehensive set of statistical methods to rigorously evaluate the performance of our approach. For long-tailed classification analysis, we used balanced accuracy to account for class imbalance on the balanced test set, and both F1 score and accuracy to assess overall performance on the test set. To determine the statistical significance of differences in performance metrics, we conducted t-tests, ensuring that observed differences were not due to random chance. Additionally, we utilized Optuna for hyperparameter optimization, leveraging its advanced algorithms to efficiently search for the best hyperparameter values and enhance model performance. For the classification experiments, we report the Matthews Correlation Coefficient (MCC), Area under the ROC Curve (AUC), and weighted F1 (wF1) scores.

5. Results

5.1 Patient Characteristics

We employ the NIH-CXR-LT and MIMIC-CXR-LT datasets for our long-tail classification task, which includes various thoracic disease pathologies alongside normal images. Based on the frequency of cases in the training set, the datasets are organized into three categories: head (more than 1,000 patients), medium (100–1,000 patients), and tail (fewer than 100 patients). In the NIH-CXR-LT dataset, the tail classes are Pneumoperitoneum, Hernia, Subcutaneous Emphysema, and Pneumomediastinum. Meanwhile, the MIMIC-CXR-LT dataset's tail classes include Pneumoperitoneum, Subcutaneous Emphysema, and Pneumomediastinum. The average age of patients in the NIH-CXR-LT training set is 46.13 $\pm$ 16.46 years, with 37,872 male patients and 30,186 female patients (Supplementary Table 6-8).

5.2 Long-tailed Classification

Here, we present the long-tailed classification results of GazeLT. Our results are compared with models trained using standard loss functions like Softmax and Focal, other standard LT baselines like Label-Distribution-Aware Margin (LDAM), re-weighting LDAM with optional deferred re-weighting (RW LDAM-DRW, and Decoupling- classifier re-training (Decoupling-cRT) (Cao et al. (2019); Cui et al. (2019)) and visual attention (VA) pre-trained baselines i.e. RadioTransformer and GazeRadar. From Table 1, we observe that, on the NIH-CXR-LT balanced set, our proposed method GazeLT outperforms LDAM by 18.2%, RW LDAM-DRW by 4.8%, and Decoupling-cRT by 4.1%. Whereas, GazeLT significantly outperforms the VA baselines RadioTransformer by 21.7% ($p<0.001$) and GazeRadar by 22.3% ($p<0.001$). Similar performance is achieved for the NIH-CXR-LT test set with GazeLT outperforming LDAM by 13.7%, RW LDAM-DRW by 2.6%, and Decoupling-cRT by 2.1%, and significantly outperforming the VA baselines RadioTransformer and GazeRadar by >15%. Similarly, for MIMIC-CXR-LT, GazeLT outperforms all baselines on the balanced set and achieves a balanced accuracy of 0.292 where the best baseline (Decoupling-cRT) achieves 0.296. It is important to note here that the proposed method It is important to note that the proposed method significantly outperforms the baseline methods on the tail classes, achieving improvements of 10.9% on the NIH-CXR-LT dataset and 12.2% on the MIMIC-CXR-LT dataset ($p < 0.001$). While GazeLT shows a slight 5% drop in head-class accuracy, it achieves significant gains in tail-class performance, which are often more clinically critical. Overall, GazeLT attains the highest average accuracy across both datasets: 0.410 on NIH-CXR-LT (13.26% improvement over the best baseline) and 0.418 on MIMIC-CXR-LT (8.01% improvement). These results highlight the model's improved diagnostic coverage across both common and rare conditions. Additional results

Table 1: **Long-Tailed Classification.** The results are shown for NIH-CXR-LT and MIMIC-CXR-LT datasets. We report average accuracy (↑) for the balanced test set and balanced accuracy (↑) for the imbalanced test set. The best and the second best results are shown in coral and light blue respectively.

Datasets(→)	**NIH-CXR-LT**					**MIMIC-CXR-LT**				
Baselines(↓)	Balanced test				Test	Balanced test				Test
	Head	Medium	Tail	Avg	bAcc	Head	Medium	Tail	Avg	bAcc
Softmax	0.419	0.056	0.017	0.164	0.115	0.503	0.039	0.022	0.188	0.169
CB Softmax	0.295	0.415	0.217	0.309	0.269	0.493	0.167	0.222	0.294	0.227
RW Softmax	0.248	0.359	0.258	0.288	0.260	0.473	0.139	0.133	0.249	0.211
Focal Loss	0.362	0.056	0.042	0.153	0.122	0.477	0.044	0.022	0.181	0.172
CB Focal Loss	0.371	0.333	0.117	0.274	0.232	0.373	0.117	0.344	0.278	0.191
RW Focal Loss	0.286	0.293	0.117	0.232	0.197	0.403	0.283	0.211	0.299	0.239
LDAM	0.410	0.133	0.142	0.228	0.178	0.497	0.000	0.000	0.166	0.165
CB LDAM	0.357	0.285	0.208	0.284	0.235	0.467	0.161	0.211	0.280	0.225
CB LDAM-DRW	0.476	0.356	0.250	0.361	0.281	0.520	0.156	0.356	0.344	0.267
RW LDAM	0.305	0.419	0.292	0.338	0.279	0.437	0.250	0.167	0.284	0.243
RW LDAM-DRW	0.410	0.367	0.308	0.362	0.289	0.447	0.256	0.311	0.338	0.275
MixUp	0.419	0.044	0.017	0.160	0.118	0.543	0.011	0.011	0.189	0.176
Balanced-MixUp	0.443	0.081	0.108	0.211	0.155	0.480	0.039	0.011	0.177	0.168
Decoupling-cRT	0.433	0.374	0.300	0.369	0.294	0.490	0.306	0.367	0.387	0.296
Decoupling-τ-norm	0.457	0.230	0.083	0.257	0.214	0.520	0.167	0.067	0.251	0.230
GazeRadar	0.390	0.074	0.075	0.187	0.140	0.527	0.006	0.000	0.279	0.174
RadioTransformer	0.386	0.093	0.083	0.193	0.131	0.493	0.0	0.0	0.260	0.164
GazeLT (Ours)	0.404	0.411	0.417	0.41	0.315	0.48	0.278	0.489	0.418	0.292

Table 2: **Ablation results.** We compare different components of the *GazeLT* architecture. We report the average accuracy (↑) for the balanced set and balanced accuracy (↑) for the imbalanced test set of NIH-CXR-LT dataset.

Components(↓)	Balanced set	Test set
Integration (I)	0.383	0.296
Disintegration (D)	0.392	0.294
TW-I	0.397	0.3
TW-D	0.377	0.299
I+D	0.363	0.295
TW-I+TW-D	0.41	0.315

Table 3: **Ablation results (MIMIC-CXR-LT).** We compare different components of the *GazeLT* architecture. We report the average accuracy (↑) for the balanced set and balanced accuracy (↑) for the imbalanced test set of MIMIC-CXR-LT dataset.

Components(↓)	Balanced set	Test set
TW-I	0.375	0.275
TW-D	0.37	0.254
TW-I+TW-D	0.418	0.292

on the individual medium classes are shown in Figure 5.A and the individual tail classes are shown in Figure 5.B.

Table 4: **Multiclass classification.** We compare GazeLT with Gazeradar and RadioTransformer. We report the balanced accuracy(↑), MCC(↑), AUC(↑) and wF1(↑) for the imbalanced test set of NIH-CXR-LT dataset. .

NIH-CXR-LT	bAcc	MCC	AUC	wF1
GazeRadar	0.187	0.175	0.791	0.17
RadioTransformer	0.193	0.197	0.79	0.183
I+D	0.363	0.337	0.821	0.316
TW-I+TW-D	0.421	0.391	0.829	0.394

5.3 Ablation

We ablate different components of GazeLT (Table 2). The teacher of GazeLT is trained using the time windowed HVAs which is a combination of TW-I and TW-D. We show that on the NIH-CXR-LT balanced test set, the balanced accuracy for the TW-I-only block is 0.397, and for the TW-D-only block is 0.377. Also, the balanced accuracy for the I-only block is 0.383, the D-only block is 0.392 and the combined I and D blocks is 0.363. Our proposed method, GazeLT (TW-I+TW-D) outperforms the combined I and D by 4.7%. This result validates our hypothesis that time window-based attention calculation improves long-tailed disease classification. We also show the ablations results on the MIMIC-CXR-LT dataset in Table 3.

Table 5: **Different windows on the balanced set (NIH-CXR-LT).**

Windows(↓)	Head	Medium	Tail	Avg
2 windows	0.348	0.396	0.408	0.382
4 windows (Ours)	0.404	0.411	0.417	0.41
8 windows	0.486	0.396	0.275	0.403

5.4 Multi-class Classification

For the NIH-CXR-LT dataset, our proposed method, GazeLT, achieves a balanced accuracy score of 0.421, outperforming GazeRadar (0.187) and RadioTransformer (0.193). In the multi-class classification task, GazeLT attains an AUC of 0.829, significantly exceeding the performance of GazeRadar (AUC: 0.791) and RadioTransformer (AUC: 0.790) (Table 4). The ROC curves for the tail classes are presented in Figure 5.C. Notably, GazeLT with TW-I+TW-D outperforms the I+D approach across all classification metrics. TW-I+TW-D achieves an MCC of 0.392, an AUC of 0.829, and a weighted F1 score of 0.394, surpassing the I+D scores of 0.337, 0.821, and 0.316, respectively.

5.5 Sensitivity Analysis of Time Window Parameter

To quantitatively evaluate the impact of temporal granularity on model performance, we conducted a sensitivity analysis by varying the number of time windows $n \in 2, 4, 8$. We report results on the balanced test set, focusing on average accuracy as well as class-group performance across head, medium, and tail categories. As summarized in Table 5, the model with $n = 4$ achieved the highest average accuracy (0.410), compared to 0.382 and 0.403 for $n = 2$ and $n = 8$, respectively. These results indicate that the 4-window configuration offers an effective trade-off between capturing sufficient temporal detail and avoiding overfitting.

To complement the quantitative findings, we visualize raw gaze points overlaid on chest X-ray images for a representative case in Rebuttal Figure 7. This example includes Atelectasis (head class) and Hiatal Hernia (tail class), marked with green and red bounding boxes, respectively (Another example in Rebuttal Figure 8). With $n = 2$, the gaze points are broadly distributed across both windows, resulting in no window distinctly capturing attention over either the head or tail class. With $n = 8$, we observe redundant attention—multiple windows contain overlapping gaze regions that cover both head and tail classes, reducing the temporal disentanglement needed for focused representation learning. In contrast, the $n = 4$ configuration demonstrates a more structured allocation of gaze, where one window primarily aligns with the head class and another aligns with the tail class. This separation enables more effective attention modeling and class-specific representation learning.

Based on these observations, we adopt $n = 4$ in all experiments throughout the paper, as it provides optimal performance while preserving interpretability and reducing redundancy in temporal attention patterns.

6. Discussions

This study introduces GazeLT, a novel deep learning framework that incorporates the temporal visual attention patterns of radiologists to improve long-tailed classification in medical imaging. Long-tailed classification is challenging due to the imbalance between common (head) and rare (tail) disease classes in medical datasets. GazeLT addresses this challenge by using a teacher-student model where the teacher is trained with radiologists' eye gaze patterns and the student model benefits from this expertise for better diagnostic accuracy.

The primary innovation of GazeLT is its focus on the temporal dynamics of visual attention. Traditional models typically use static aggregated attention maps, but this study decomposes visual attention into time-windowed segments, capturing the dynamic nature of radiologists' gaze patterns. This temporal resolution allows the DL model to replicate the sequential and hierarchical nature of visual search patterns, leading to better performance in disease classification.

Incorporating clinician-in-the-loop strategies significantly enhances the interpretability of DL models. Radiologists' eye gaze patterns provide clinically relevant cues that guide the model's focus towards important regions in the medical images. This alignment with human experts' decision-making processes not only improves diagnostic accuracy but also offers a more transparent rationale for the model's predictions. This is crucial as DL models in radiology often learn shortcuts or focus on irrelevant features, leading to potential misdiagnoses.

Previous works on long-tailed learning have focused on mitigating class imbalance through methods like reweighting, class balancing, and decoupling (Cao et al. (2019); Cui et al. (2019)) often relying on modified loss functions. In contrast, this study introduces a novel teacher-student framework that integrates radiologists' gaze-based visual attention patterns to address long-tailed disease classification. We retain the original loss function and enhance learning by aligning model attention with expert cues. This is the first work to leverage human visual attention in a time-windowed paradigm, offering a unique perspective for improving model performance in imbalanced medical datasets.

The teacher-student framework of GazeLT ensures that the student model inherits the nuanced understanding of rare disease patterns from the teacher model, which is trained with the time-windowed visual attention data. Experiments

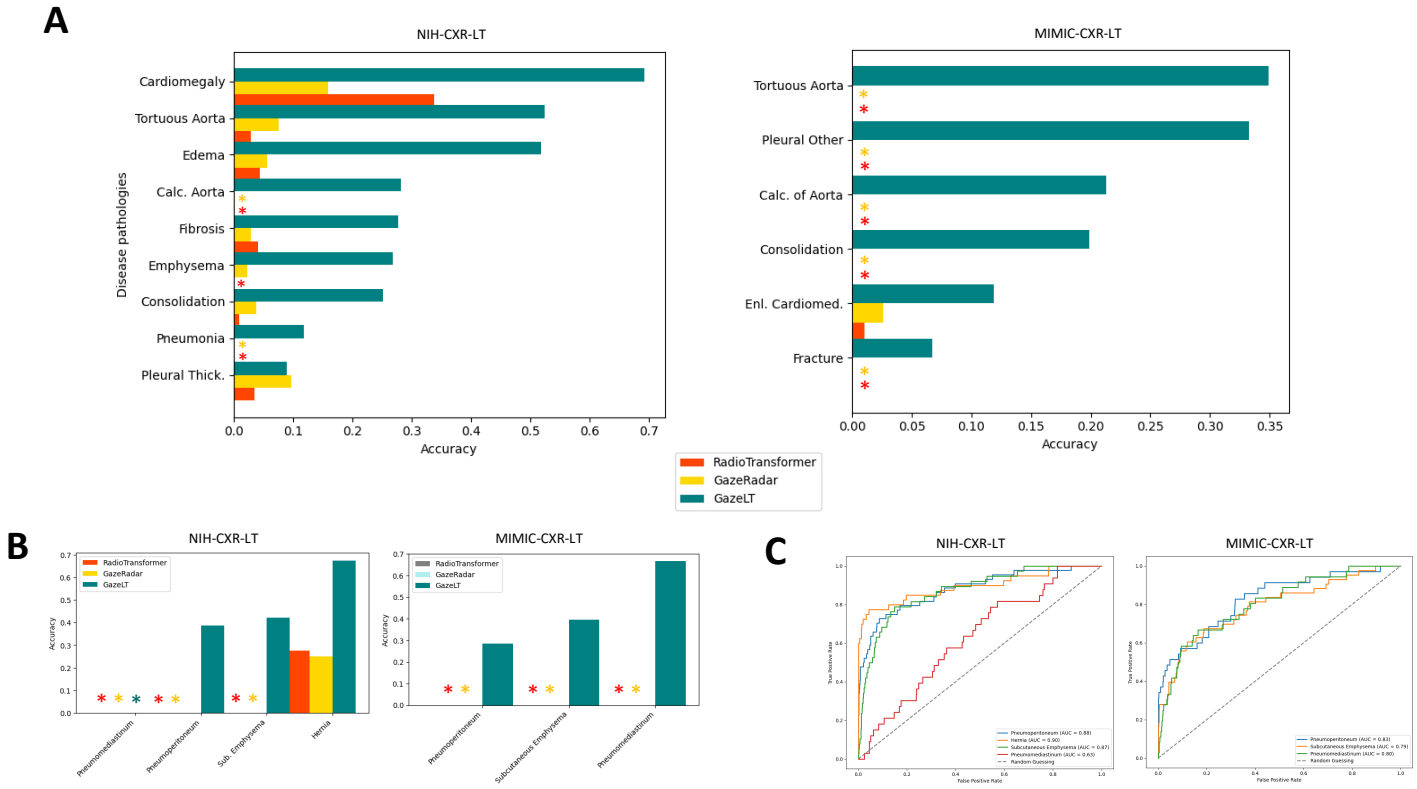

Figure 5: A. Accuracy of medium classes on NIH-CXR-LT and MIMIC-CXR-LT datasets, comparing GazeLT, GazeRadar, and RadioTransformer, B. Accuracy of tail classes on NIH-CXR-LT and MIMIC-CXR-LT datasets, comparing GazeLT, GazeRadar, and RadioTransformer (* represents 0), C. ROC-AUC curves for tail classes on NIH-CXR-LT and MIMIC-CXR-LT datasets.

on both datasets demonstrate that GazeLT consistently outperforms baseline models, particularly in identifying tail classes. The comparative analysis shows significant improvements in balanced accuracy and F1 scores across both head and tail classes, outperforming models like RadioTransformer and GazeRadar that lack the temporal dynamics and comprehensive integration strategies of GazeLT.

Ablation studies further validate the contributions of the individual components of GazeLT. The superior performance of the combined TW-I and TW-D blocks over their standalone counterparts emphasizes the importance of both fine-grained and coarse attention patterns. The significant performance drop observed when these components are excluded or simplified further confirms that the integration of both attention strategies is essential for effective long-tailed classification.

A key strength of our proposed GazeLT architecture is its efficient use of radiologists' eye gaze data, which is required only during the training of the teacher model. During inference, the model relies solely on the input image, significantly reducing computational overhead and precluding the need for additional eye gaze data accrual. Furthermore, unlike previous approaches that focus on single time-point attention, our method captures detailed, time-windowed gaze information, enabling a more comprehensive understanding of visual attention dynamics.

While *GazeLT* demonstrates strong performance in long-tailed chest X-ray classification, it has certain limitations. A central dependency of the proposed framework is the availability of radiologist eye-tracking data during training, which may pose practical challenges related to data acquisition, standardization, and scalability. The collection of high-quality gaze fixation points requires dedicated eye-tracking hardware, controlled viewing conditions, and participation from expert clinicians—factors that may limit widespread adoption, particularly across institutions with varying resources and infrastructure. Importantly, however, gaze data is only utilized during the training phase to supervise the teacher network. Once the knowledge distillation process is complete, the student model operates independently and does not require gaze input at inference time. This design ensures that the deployment of *GazeLT* remains feasible in clinical environments where eye-tracking data is unavailable.

Moreover, while our experiments focus exclusively on chest radiographs, the broader applicability of *GazeLT* to other imaging modalities (e.g., CT, MRI, ultrasound) and clinical tasks (e.g., lesion detection, segmentation) remains an open question. In previous studies, eye gaze patterns collected from 3D brain MRIs have been leveraged for segmentation tasks. In our proposed framework, we demonstrate that eye gaze data acquired from 2D chest X-rays significantly improves performance on long-tailed classification. While our current work focuses on 2D data, the approach is readily extensible to other imaging modalities, including 3D scans and videos. Although collecting eye gaze data for 3D images poses practical challenges, prior works have already established feasibility by successfully acquiring such data. Hence, our method is inherently modality-agnostic and can be readily extended to diverse imaging modalities, including 2D, 3D, and dynamic (video) data. Additionally, the complexity of the teacher-student framework may increase computational requirements. Future work could explore the applicability of GazeLT across different medical imaging modalities and the integration of multi-modal data to further enhance diagnostic accuracy and interpretability. Moreover, investigating the applicability of this approach to other domains with long-tailed distributions could provide broader insights into the potential of temporal visual attention in DL models.

In summary, GazeLT represents a significant advancement in medical imaging by integrating the temporal visual attention patterns of radiologists into a DL framework. This approach improves the interpretability and clinical relevance of model predictions and addresses the challenges of long-tailed classification. The study demonstrates the importance of temporal dynamics in visual attention-based learning. As the field of medical AI evolves, incorporating expert knowledge into DL models will be crucial for developing robust, accurate, and interpretable diagnostic tools.

7. Conclusion

In this work, we present a visual attention-guided deep learning framework for long-tailed classification. Experts' temporal visual attention consists of context-rich *integration* attention and coarse *disintegration* attention. These attentions, captured at different time windows, when learned by transformer architectures, generate better visual attention-guided representations. At different time windows, the radiologists look at different disease patterns ranging from the *head* classes to the *tail* classes. These representations help in improving performance in long-tailed disease classification. One of the major limitations of our work is that we do not take into consideration the diagnosis confidence score of radiologists to compute the time windows. In the future, we aim to work on combining multiple radiologists' gaze patterns for long-tailed disease classification and evaluate the effect of changing the time windows.

Acknowledgements

This research was partially supported by National Institutes of Health (NIH) and National Cancer Institute (NCI) grants 1R21CA258493-01A1, 1R01CA297843-01, 3R21CA258493-02S1, 1R03DE033489-01A1, and National Science Foundation (NSF) grant 2442053. The content is solely the responsibility of the authors and does not necessarily represent the official views of the National Institutes of Health.

Data availability

The datasets used in this study are publicly available. The EDG-CXR dataset is available at this PhysioNet link, and the REFLACX dataset is available at this PhysioNet link. The chest X-ray (CXR) images are obtained from the MIMIC-CXR-JPG dataset, which is available at the PhysioNet link. The long-tailed classification datasets, NIH-CXR-LT and MIMIC-CXR-LT, are available at this GitHub repository.

References

Sabrina Amrouche, Benedikt Gollan, Alois Ferscha, and Josef Heftberger. Activity segmentation and identification based on eye gaze features. In *Proceedings of the 11th Pervasive Technologies Related to Assistive Environments Conference*, pages 75–82, 2018.

Moinak Bhattacharya and Prateek Prasanna. Gazediff: A radiologist visual attention guided diffusion model for zero-shot disease classification. In *Medical Imaging with Deep Learning*, 2024.

Moinak Bhattacharya, Shubham Jain, and Prateek Prasanna. Gazeradar: A gaze and radiomics-guided disease localization framework. In *International Conference on Medical Image Computing and Computer-Assisted Intervention*, pages 686–696. Springer, 2022a.

Moinak Bhattacharya, Shubham Jain, and Prateek Prasanna. Radiotransformer: a cascaded global-focal transformer for visual attention–guided disease classification. In *European Conference on Computer Vision*, pages 679–698. Springer, 2022b.

Moinak Bhattacharya, Gagandeep Singh, Shubham Jain, and Prateek Prasanna. Radgazegen: Radiomics and gaze-guided medical image generation using diffusion models. *arXiv preprint arXiv:2410.00307*, 2024.

Kaidi Cao, Colin Wei, Adrien Gaidon, Nikos Arechiga, and

Tengyu Ma. Learning imbalanced datasets with label-distribution-aware margin loss. *Advances in neural information processing systems*, 32, 2019.

Dae-Yong Cho and Min-Koo Kang. Human gaze-aware attentive object detection for ambient intelligence. *Engineering Applications of Artificial Intelligence*, 106:104471, 2021.

Rosie Clark, James Blundell, Matt J Dunn, Jonathan T Erichsen, Mario E Giardini, Irene Gottlob, Chris Harris, Helena Lee, Lee Mcilreavy, Andrew Olson, et al. The potential and value of objective eye tracking in the ophthalmology clinic. *Eye*, 33(8):1200–1202, 2019.

François Courtemanche, Esma Aïmeur, Aude Dufresne, Mehdi Najjar, and Franck Mpondo. Activity recognition using eye-gaze movements and traditional interactions. *Interacting with Computers*, 23(3):202–213, 2011.

Yin Cui, Menglin Jia, Tsung-Yi Lin, Yang Song, and Serge Belongie. Class-balanced loss based on effective number of samples. In *Proceedings of the IEEE/CVF conference on computer vision and pattern recognition*, pages 9268–9277, 2019.

Kevin Conrad Dieter and Duje Tadin. Understanding attentional modulation of binocular rivalry: a framework based on biased competition. *Frontiers in Human Neuroscience*, 5:155, 2011.

Trafton Drew, Sage EP Boettcher, and Jeremy M Wolfe. One visual search, many memory searches: An eye-tracking investigation of hybrid search. *Journal of vision*, 17(11):5–5, 2017.

Charles Elkan. The foundations of cost-sensitive learning. In *International joint conference on artificial intelligence*, volume 17, pages 973–978. Lawrence Erlbaum Associates Ltd, 2001.

Andrew Estabrooks, Taeho Jo, and Nathalie Japkowicz. A multiple resampling method for learning from imbalanced data sets. *Computational intelligence*, 20(1):18–36, 2004.

Jean Feng, Rachael V Phillips, Ivana Malenica, Andrew Bishara, Alan E Hubbard, Leo A Celi, and Romain Pirracchio. Clinical artificial intelligence quality improvement: towards continual monitoring and updating of ai algorithms in healthcare. *NPJ digital medicine*, 5(1):66, 2022.

Ruiwei Feng, Xiangshang Zheng, Tianxiang Gao, Jintai Chen, Wenzhe Wang, Danny Z Chen, and Jian Wu. Interactive few-shot learning: Limited supervision, better medical image segmentation. *IEEE Transactions on Medical Imaging*, 40(10):2575–2588, 2021.

Joao Filipe Ferreira and Jorge Dias. Attentional mechanisms for socially interactive robots–a survey. *IEEE Transactions on Autonomous Mental Development*, 6(2): 110–125, 2014.

Adrian Galdran, Gustavo Carneiro, and Miguel A González Ballester. Balanced-mixup for highly imbalanced medical image classification. In *Medical Image Computing and Computer Assisted Intervention–MICCAI 2021: 24th International Conference, Strasbourg, France, September 27–October 1, 2021, Proceedings, Part V 24*, pages 323–333. Springer, 2021.

Gregory Holste, Song Wang, Ziyu Jiang, Thomas C Shen, George Shih, Ronald M Summers, Yifan Peng, and Zhangyang Wang. Long-tailed classification of thorax diseases on chest x-ray: A new benchmark study. In *MICCAI Workshop on Data Augmentation, Labelling, and Imperfections*, pages 22–32. Springer, 2022.

Muhammad Abdullah Jamal, Matthew Brown, Ming-Hsuan Yang, Liqiang Wang, and Boqing Gong. Rethinking class-balanced methods for long-tailed visual recognition from a domain adaptation perspective. In *Proceedings of the IEEE/CVF conference on computer vision and pattern recognition*, pages 7610–7619, 2020.

Adam James, D Vieira, Benny Lo, Ara Darzi, and G Z Yang. Eye-gaze driven surgical workflow segmentation. In *Medical Image Computing and Computer-Assisted Intervention–MICCAI 2007: 10th International Conference, Brisbane, Australia, October 29-November 2, 2007, Proceedings, Part II 10*, pages 110–117. Springer, 2007.

Muwei Jian, Jing Wang, Hui Yu, Guodong Wang, Xianjing Meng, Lu Yang, Junyu Dong, and Yilong Yin. Visual saliency detection by integrating spatial position prior of object with background cues. *Expert Systems with Applications*, 168:114219, 2021.

Lie Ju, Xin Wang, Lin Wang, Tongliang Liu, Xin Zhao, Tom Drummond, Dwarikanath Mahapatra, and Zongyuan Ge. Relational subsets knowledge distillation for long-tailed retinal diseases recognition. In *Medical Image Computing and Computer Assisted Intervention–MICCAI 2021: 24th International Conference, Strasbourg, France, September 27–October 1, 2021, Proceedings, Part VIII 24*, pages 3–12. Springer, 2021.

Robert H Logie. Spatial and visual working memory: A mental workspace. In *Psychology of learning and motivation*, volume 42, pages 37–78. Elsevier, 2003.

Chong Ma, Lin Zhao, Yuzhong Chen, Sheng Wang, Lei Guo, Tuo Zhang, Dinggang Shen, Xi Jiang, and Tianming Liu.

Eye-gaze-guided vision transformer for rectifying shortcut learning. *IEEE Transactions on Medical Imaging*, 2023.

Stefan Mathe and Cristian Sminchisescu. Actions in the eye: Dynamic gaze datasets and learnt saliency models for visual recognition. *IEEE transactions on pattern analysis and machine intelligence*, 37(7):1408–1424, 2014.

Kyle Min and Jason J Corso. Integrating human gaze into attention for egocentric activity recognition. In *Proceedings of the IEEE/CVF Winter Conference on Applications of Computer Vision*, pages 1069–1078, 2021.

Wongi Park, Inhyuk Park, Sungeun Kim, and Jongbin Ryu. Robust asymmetric loss for multi-label long-tailed learning. In *Proceedings of the IEEE/CVF international conference on computer vision*, pages 2711–2720, 2023.

Angshuman Paul, Thomas C Shen, Sungwon Lee, Niranjan Balachandar, Yifan Peng, Zhiyong Lu, and Ronald M Summers. Generalized zero-shot chest x-ray diagnosis through trait-guided multi-view semantic embedding with self-training. *IEEE Transactions on Medical Imaging*, 40 (10):2642–2655, 2021.

Jiawei Ren, Cunjun Yu, Xiao Ma, Haiyu Zhao, Shuai Yi, et al. Balanced meta-softmax for long-tailed visual recognition. *Advances in neural information processing systems*, 33:4175–4186, 2020.

Mona P Roshan, Jacklyn Garcia, Ana B Cury, Chrisnel Lamy, Frederico Souza, Charif Sidani, and Ricardo C Cury. Eye tracking validation: Improving radiologist reporting and interpretation. *European Journal of Radiology*, 168: 111134, 2023.

Santanu Roy, Mrinal Tyagi, Vibhuti Bansal, and Vikas Jain. Svd-clahe boosting and balanced loss function for covid-19 detection from an imbalanced chest x-ray dataset. *Computers in Biology and Medicine*, 150:106092, 2022.

Zohaib Salahuddin, Henry C Woodruff, Avishek Chatterjee, and Philippe Lambin. Transparency of deep neural networks for medical image analysis: A review of interpretability methods. *Computers in biology and medicine*, 140:105111, 2022.

Nataliya Shapovalova, Michalis Raptis, Leonid Sigal, and Greg Mori. Action is in the eye of the beholder: Eye-gaze driven model for spatio-temporal action localization. *Advances in Neural Information Processing Systems*, 26, 2013.

Ran Shi, Ngi King Ngan, and Hongliang Li. Gaze-based object segmentation. *IEEE Signal Processing Letters*, 24 (10):1493–1497, 2017.

Boris Shirokikh, Alexey Shevtsov, Anvar Kurmukov, Alexandra Dalechina, Egor Krivov, Valery Kostjuchenko, Andrey Golanov, and Mikhail Belyaev. Universal loss reweighting to balance lesion size inequality in 3d medical image segmentation. In *Medical Image Computing and Computer Assisted Intervention–MICCAI 2020: 23rd International Conference, Lima, Peru, October 4–8, 2020, Proceedings, Part IV 23*, pages 523–532. Springer, 2020.

Brian A Smith, Qi Yin, Steven K Feiner, and Shree K Nayar. Gaze locking: passive eye contact detection for human-object interaction. In *Proceedings of the 26th annual ACM symposium on User interface software and technology*, pages 271–280, 2013.

Mohammed Tahri Sqalli et al. Understanding cardiology practitioners' interpretations of electrocardiograms: An eye-tracking study. *JMIR Human Factors*, 9(1):e34058, 2022.

Joseph N Stember, Haydar Celik, David Gutman, Nathaniel Swinburne, Robert Young, Sarah Eskreis-Winkler, Andrei Holodny, Sachin Jambawalikar, Bradford J Wood, Peter D Chang, et al. Integrating eye tracking and speech recognition accurately annotates mr brain images for deep learning: proof of principle. *Radiology: Artificial Intelligence*, 3(1):e200047, 2020.

Ellhia Sudin, Mitchell Searjeant, George Partridge, Peter Phillips, Louise Hiller, David Snead, Ian Ellis, and Yan Chen. Digital pathology: the effect of experience on visual search behavior. *Journal of Medical Imaging*, 9(3): 035501–035501, 2022.

Mohammed Tahri Sqalli et al. Interpretation of a 12-lead electrocardiogram by medical students: quantitative eye-tracking approach. *JMIR medical education*, 7(4):e26675, 2021.

Jingru Tan, Changbao Wang, Buyu Li, Quanquan Li, Wanli Ouyang, Changqing Yin, and Junjie Yan. Equalization loss for long-tailed object recognition. In *Proceedings of the IEEE/CVF conference on computer vision and pattern recognition*, pages 11662–11671, 2020.

Jingru Tan, Xin Lu, Gang Zhang, Changqing Yin, and Quanquan Li. Equalization loss v2: A new gradient balance approach for long-tailed object detection. In *Proceedings of the IEEE/CVF conference on computer vision and pattern recognition*, pages 1685–1694, 2021.

A Van der Gijp, CJ Ravesloot, H Jarodzka, MF Van der Schaaf, IC Van der Schaaf, Jan PJ van Schaik, and Th J Ten Cate. How visual search relates to visual diagnostic performance: a narrative systematic review of

eye-tracking research in radiology. *Advances in Health Sciences Education*, 22:765–787, 2017.

Bin Wang, Armstrong Aboah, Zheyuan Zhang, and Ulas Bagci. Gazesam: What you see is what you segment. *arXiv preprint arXiv:2304.13844*, 2023.

Bin Wang, Hongyi Pan, Armstrong Aboah, Zheyuan Zhang, Elif Keles, Drew Torigian, Baris Turkbey, Elizabeth Krupinski, Jayaram Udupa, and Ulas Bagci. Gazegnn: A gaze-guided graph neural network for chest x-ray classification. In *Proceedings of the IEEE/CVF Winter Conference on Applications of Computer Vision*, pages 2194–2203, 2024.

Tao Wang, Yu Li, Bingyi Kang, Junnan Li, Junhao Liew, Sheng Tang, Steven Hoi, and Jiashi Feng. The devil is in classification: A simple framework for long-tail instance segmentation. In *Computer Vision–ECCV 2020: 16th European Conference, Glasgow, UK, August 23–28, 2020, Proceedings, Part XIV 16*, pages 728–744. Springer, 2020.

Michael Yeung, Evis Sala, Carola-Bibiane Schönlieb, and Leonardo Rundo. Unified focal loss: Generalising dice and cross entropy-based losses to handle class imbalanced medical image segmentation. *Computerized Medical Imaging and Graphics*, 95:102026, 2022.

Guanghui Yue, Peishan Wei, Tianwei Zhou, Qiuping Jiang, Weiqing Yan, and Tianfu Wang. Toward multicenter skin lesion classification using deep neural network with adaptively weighted balance loss. *IEEE Transactions on Medical Imaging*, 42(1):119–131, 2022.

Li Zhang, Xin Wen, Jian-Wei Li, Xu Jiang, Xian-Feng Yang, and Meng Li. Diagnostic error and bias in the department of radiology: a pictorial essay. *Insights into Imaging*, 14 (1):163, 2023a.

Ruru Zhang, E Haihong, Lifei Yuan, Jiawen He, Hongxing Zhang, Shengjuan Zhang, Yanhui Wang, Meina Song, and Lifei Wang. Mbnm: multi-branch network based on memory features for long-tailed medical image recognition. *Computer Methods and Programs in Biomedicine*, 212:106448, 2021.

Yifan Zhang, Bingyi Kang, Bryan Hooi, Shuicheng Yan, and Jiashi Feng. Deep long-tailed learning: A survey. *IEEE Transactions on Pattern Analysis and Machine Intelligence*, 2023b.

Zizhao Zhang and Tomas Pfister. Learning fast sample re-weighting without reward data. In *Proceedings of the IEEE/CVF International Conference on Computer Vision*, pages 725–734, 2021.

S Kevin Zhou, Hayit Greenspan, Christos Davatzikos, James S Duncan, Bram Van Ginneken, Anant Madabhushi, Jerry L Prince, Daniel Rueckert, and Ronald M Summers. A review of deep learning in medical imaging: Imaging traits, technology trends, case studies with progress highlights, and future promises. *Proceedings of the IEEE*, 109(5):820–838, 2021.

Appendix A. Inclusion and Exclusion criteria

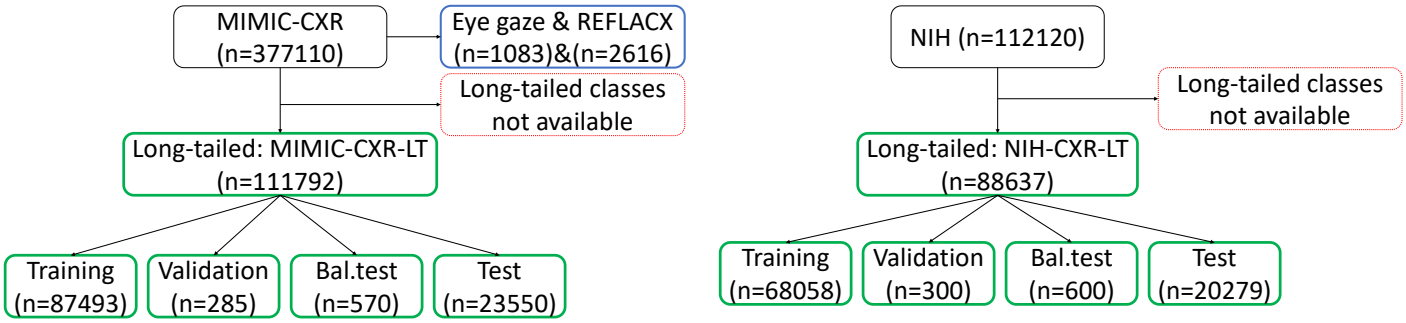

Figure 6: Inclusion-Exclusion criteria.

Appendix B. Patient demographics

Type	Class	n
Head	No Finding	45439
	Infiltration	6941
	Atelectasis	3135
	Effusion	2875
	Nodule	2036
	Mass	1665
	Pneumothorax	1485
Medium	Consolidation	868
	Pleural Thickening	811
	Cardiomegaly	800
	Fibrosis	519
	Edema	435
	Tortuous Aorta	339
	Emphysema	229
	Pneumonia	213
	Calcification of the Aorta	121
Tail	Pneumoperitoneum	59
	Hernia	49
	Subcutaneous Emphysema	32
	Pneumomediastinum	7

Table 6: NIH-CXR-LT

Type	Class	n
Head	No Finding	53260
	Lung Opacity	7927
	Cardiomegaly	5113
	Atelectasis	4539
	Pleural Effusion	3832
	Support Devices	3279
	Edema	2395
	Pneumonia	2195
	Pneumothorax	1172
	Lung Lesion	1036
Medium	Fracture	791
	Enlarged Cardiomediastinum	638
	Consolidation	609
	Pleural Other	254
	Calcification of the Aorta	207
	Tortuous Aorta	175
Tail	Pneumoperitoneum	32
	Subcutaneous Emphysema	27
	Pneumomediastinum	12

Table 7: MIMIC-CXR-LT

Parameters	Categories	n
Gender	Male	37872
	Female	30186
Age	<20	4426
	20-30	7841
	30-40	10498
	50-60	16391
	70-80	3602
	80-90	529
	90-100	27

Table 8: Demographics

Appendix C. Additional Qualitative Results

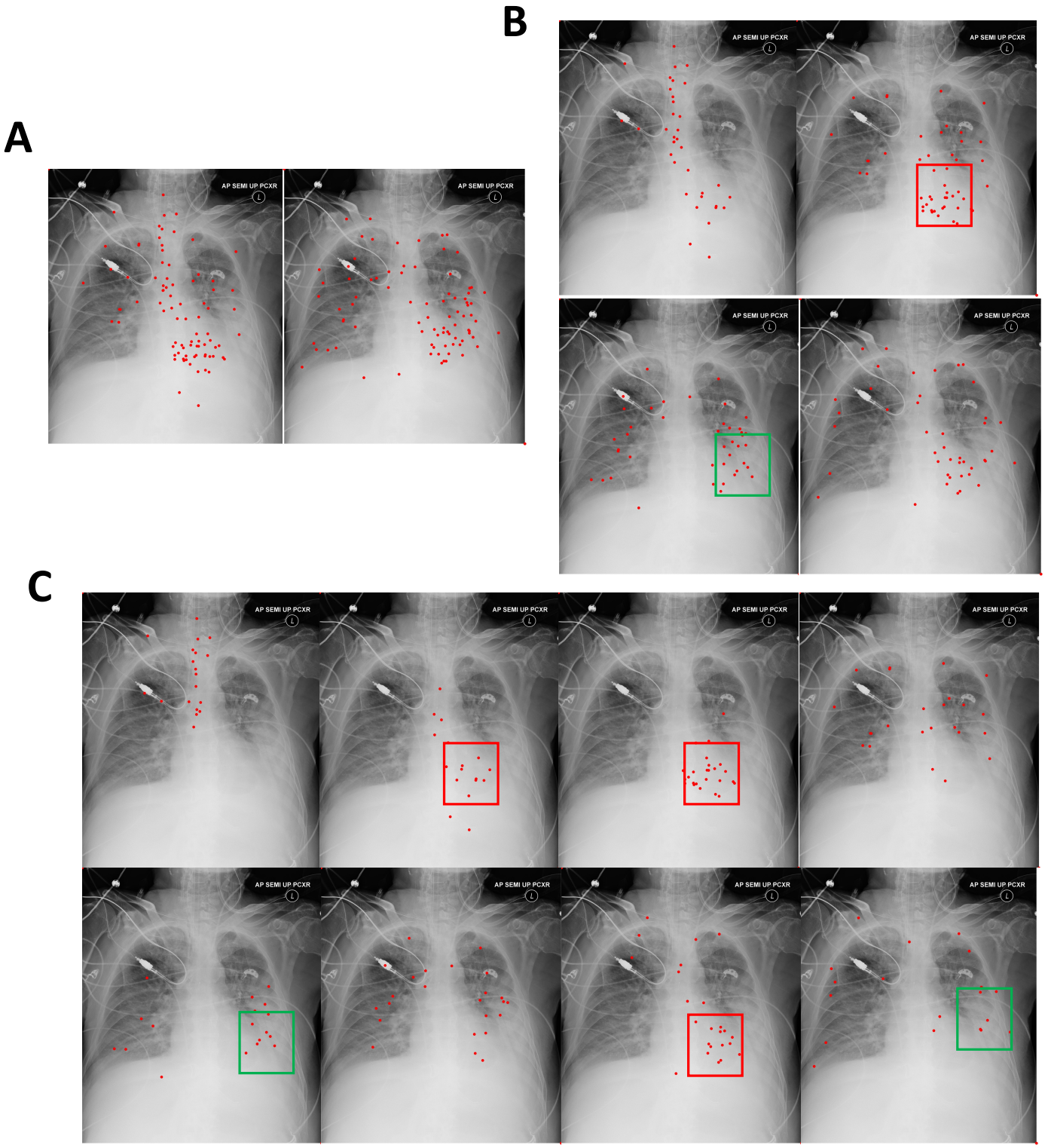

Figure 7: **Gaze point temporal alignment with head and tail class regions across different time window divisions.** (A) Example of a patient with atelectasis (head class) and hiatal hernia (tail class). Gaze points are divided into two time windows, but neither window shows fixation on the relevant class regions. (B) Gaze points divided into four time windows. This represents an ideal temporal separation: the head class region (red bounding box) and tail class region (green bounding box) are fixated in distinct time windows. (C) Gaze points divided into eight time windows. Both head and tail class regions receive attention in multiple windows, indicating temporally overlapping focus across classes.

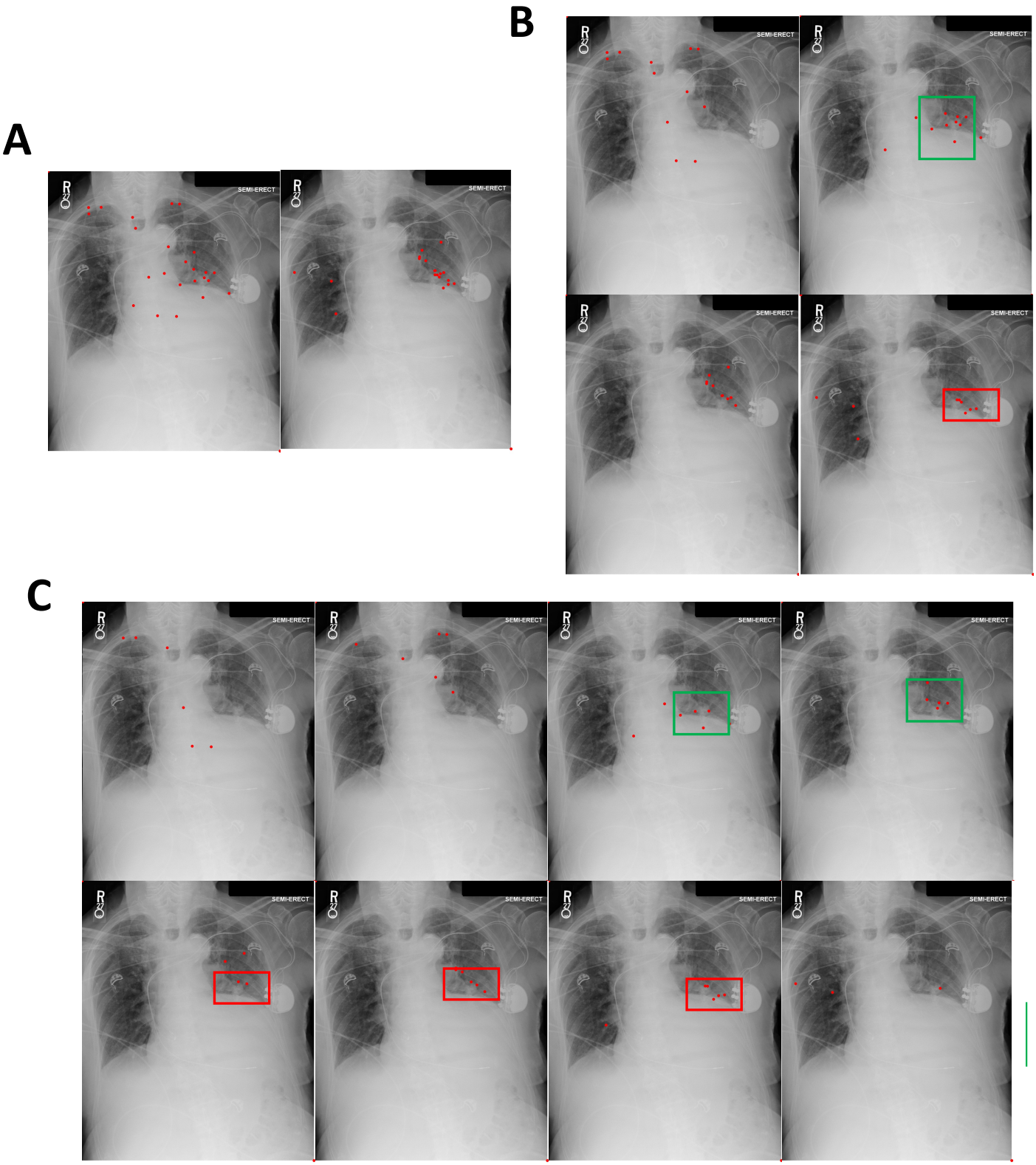

Figure 8: **Additional qualitative results.** Example of another patient with atelectasis (head class) and enlarged hilum (tail class).

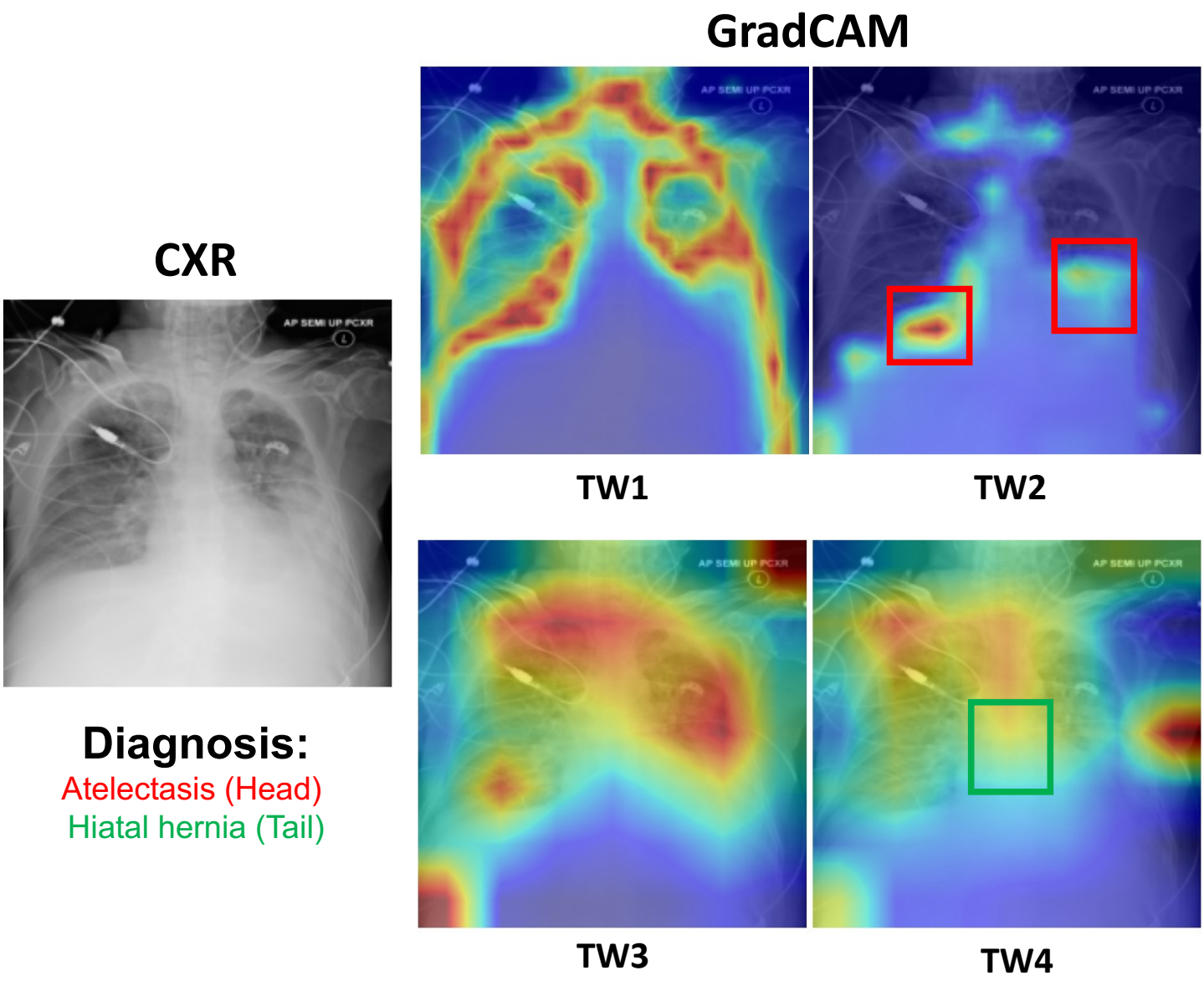

Figure 9: Visualization of gaze and model attention for a patient diagnosed with Atelectasis (head class) and Hiatal Hernia (tail class). GradCAM heatmaps from the model predictions are included for comparison. Radiologist-annotated regions corresponding to the head class are shown with red bounding boxes, and tail class regions with green bounding boxes.